

Inverse Design of Mechanical Metamaterials Using a Point-Cloud-Based Deep Generative Model

Seungwook Hong^{1†}, Kijung Kim^{1†}, Wonjun Jung¹, Wooseok Kim¹, Namjung Kim^{2*}, and Howon Lee^{1*}

¹Department of Mechanical Engineering, Institute of Advanced Machines and Design, Seoul National University, Seoul, Republic of Korea

²Department of Mechanical Engineering, Gachon University, Sungnam, Republic of Korea

†These authors contributed equally.

*Corresponding author (e-mail: namjungk@gachon.ac.kr, howon.lee@snu.ac.kr)

Abstract

Mechanical metamaterials have garnered attention for their engineered mechanical properties, enabling control over specific behaviors. Advances in additive manufacturing have expanded design freedom for complex metamaterials. However, the design process remains challenging due to vast design space and numerous parameters. While artificial intelligence (AI) aids design, current approaches are often restricted to predefined, parameterized structures. This study introduces a parameter-free design strategy for 3D mechanical metamaterials using point-cloud-based deep generative networks. A library of widely known metamaterial structures was constructed to train the machine learning model. The trained latent space forms clusters of unit cell topologies with similar properties, enabling efficient exploration and smooth interpolation. Additionally, mechanical properties can be predicted more faster than with conventional methods. This approach created metamaterials with targeted properties, unrestricted by parameterized constraints. Computational and experimental validations confirmed alignment with desired properties within acceptable error margins. We believe this work significantly enhances design flexibility in AI-driven metamaterials, expanding their potential applications across various fields.

Keywords: 3D Metamaterial, Deep generative model, Point cloud structure, Transition Unit cell

Introduction

Metamaterials are specially engineered structures designed to exhibit properties not found in nature. Their unique characteristics arise from their internal microstructures, rather than the substances they are made of. Among these, mechanical metamaterials specifically manipulate the geometric arrangement of their microstructures to achieve unusual mechanical properties, such as enhanced strength or flexibility. These structures typically consist of microlattices with periodically arranged unit cells. Various microlattices exhibit unique characteristics not seen in conventional materials, such as lightweight structures with high strength [1, 2], negative Poisson's ratios [3, 4], and negative coefficients of thermal expansion [5]. While traditional manufacturing methods such as injection molding and machining had difficulties in fabricating such microlattice structures, the advancements in additive manufacturing (AM) technology now allow for the precise creation of complex microstructures across a wide range of scales, from tens of micrometers to several centimeters [1]. The unique capability of AM that allows for easy and rapid production of complex 3D geometries offers a high degree of design freedom, which has triggered extensive exploration of diverse topologies and structures with exotic properties in the past decade [6].

Designing microlattice structures, despite their significant applications and vast potential, presents considerable challenges. Traditional approaches to designing microlattices include theoretical analysis [7, 8], topology optimization [9, 10], and bioinspired designs [11]. Theoretical analysis is based on traditional mechanics for designing relatively simple structures. Topology optimization iteratively finds the optimal design by considering various conditions and performing hundreds of iterations within a given design space. Bioinspiration emulates the designs found in nature. However, these methods require the designer's extensive prior knowledge in mechanics and often involve many trials and errors during the design process. They are also often constrained

by significant computational demands and extended processing times, which become particularly challenging for intricate designs. Furthermore, considering various conditions in designing complex structures, these methods are often inefficient and do not always yield the most optimal results.

Recently, machine learning (ML) has been extensively studied and employed across various fields of research [12-22]. In particular, ML rapidly discovers and learns complex rules or patterns from large-scale data, significantly enhancing the efficiency of designing new structures. Lee et al. [14] proposed a generative machine learning algorithm for lattice structures with superior mechanical properties. It introduced an innovative approach combining neural networks with genetic algorithms, generating novel lattice structures in body-centered cubic forms that depart from traditional cylindrical struts with circular cross-sections, thus producing structures with the targeted mechanical properties. In another study, Eren et al. [16] generated data for 3D lattice unit cells with varying geometric parameters, which they used to train GANs for optimizing the mechanical properties and load-carrying capacity of SLM-manufactured lattice structures. The researchers then used this data to train Generative Adversarial Networks (GANs), significantly enhancing the load-carrying capacity of optimized 3D lattice structures. Similarly, Zheng et al. [18] developed a three-dimensional conditional Generative Adversarial Network (3D-CGAN) using voxelized Voronoi lattice data aimed at designing architected cellular materials with precise porosity and stiffness specifications. Recent computational advancements, as discussed by Bonfanti et al. [21], further highlight how machine learning and optimization methods have enabled the design of intricate mechanical metamaterials, significantly pushing the boundaries of traditional approaches. Their approach efficiently generates new geometries with targeted mechanical properties. Despite the significant advances these studies represent, there are inherent

challenges that need to be addressed. For instance, handling 3D voxel data necessitates substantial computational resources due to the large dataset sizes, requiring powerful computing systems for effective training. Additionally, the use of predefined parameters in creating training data could limit the diversity of structures generated, leading to restricted design freedom. Furthermore, proper connectivity within the microstructure is essential as it significantly influences the structural integrity and manufacturability of the designs.

In this study, we present a deep generative network for the parameter-free design of mechanical metamaterials with targeted mechanical properties. This study adopts point cloud representation to express the 3D structure, leveraging its advantages in handling complex geometries and enabling diverse structural designs. We create a diverse point-cloud dataset from widely known 3D lattice geometries, labeled using a homogenization method. This deep generative network, based on a variational autoencoder, is trained to enable the rapid design of new unit cell topologies with desired properties through simple linear interpolation. It facilitates smooth transitions between predefined parameterized shapes, allowing for the generation of novel topologies beyond the initial dataset. We validated the newly generated designs through both computational and experimental methods. After fabricating the structures via 3D printing, we conducted experimental testing, confirming that their mechanical properties were within acceptable error margins of the desired specifications. Overall, this method provides an efficient pathway for designing mechanical metamaterials with targeted property requirements, expanding its applicability beyond mechanical performance.

Results

3D structure data type

In order to effectively train a VAE model, the selection of the most suitable training data is important. Among various factors, the first and most crucial aspect is choosing an appropriate data type that accurately represents 3D structures for the training process. This decision is fundamental to the model's learning effectiveness and overall performance. Regarding this, there are various types of 3D data representations such as voxel [23, 24], graph [25, 26], and point cloud [27-31]. Voxel representation divides the 3D space into uniformly sized grids, assigning a value of 1 to solid parts and 0 to voids within each grid. Although it enables the representation of various structures in a uniform size of data, it demands substantially increased computational memory capacity as the data complexity increases. Graph-based representation is composed of nodes and their connecting edges. It allows for a concise expression of only the structure-related parts, resulting in a smaller data size. Despite its efficiency, it has limitations in representing complex structures that are not of the strut type. This approach also results in a limited design space due to the assumption of uniform strut thickness for each edge. Point cloud is represented as set of 3d points of the given geometry and contains coordinate information for each point. Unlike graph-based representation, point cloud does not have connectivity information between points, requiring additional processes for reconstructing the original structure. Nevertheless, since it can easily represent complex structures, it could design diverse geometries without structural constraints. Considering these factors, this work employs the point cloud representation for training the VAE model.

Data generation process

Following data type selection, we generated data as input for the model. For the six unit-cell geometries shown in Figure 2(A), we generated a total of 10,000 point cloud data for each of the following structures: body-centered cubic (BCC), cubic, octahedron, octet-truss, kelvin foam, and fluorite. This was achieved by varying design parameters such as the overall size of the structure and the radius of the struts. The datasets were subsequently preprocessed to serve as training data. Figure 2(B) shows the process of data generation in the case of BCC. We chose three data parameters to represent a BCC: a , b , and r . Parameters a and b are related to the size of the unit cell, where the length is fixed at 30, and the width and height correspond to a and b , respectively. The values of a and b range between even numbers from 16 to 60, corresponding to sizes ranging from half to twice the fixed length of 30. The parameter r is related to the strut radius. In the case of BCC structures, considering symmetry, there is only one type of strut as shown in Figure 2(B), leading to a single value for r . The value of r ranges between 1 and 3. Firstly, the structure is composed in a wireframe line form, with the BCC configuration consisting of four diagonal lines. Following this, the voxelization process is applied, where each point in the grid is evaluated. If the distance to the nearest line is smaller than the strut radius, those points are included in the structure-forming point cloud data. This voxel data represents the geometry of the BCC structure. Therefore, once parameters a , b , and r are determined, a single BCC structure point cloud data is generated. By assigning random values to a , b , and r , we generated a total of 10,000 point cloud datasets. During the preprocessing step of the point cloud data generated for training, we reduced the data size by 1/8 considering the symmetry of the BCC unit cell. Since each data set has a different structural size, we normalized the sizes by applying uniform scaling. This involved centering the structures at the origin and resizing them so they could be accommodated

within a unit cube. Additionally, as the number of points included in each data varies, a padding process was applied. Within each dataset, the process involved selectively duplicating and adding points that are farthest from the origin, thereby ensuring that each dataset achieves the maximum number of points at dataset. This specific approach was chosen instead of zero-padding, as zero-padding introduces zero points that are not present in the original data, which could lead to less effective reconstruction. By duplicating and adding points farthest from the origin, we maintain the integrity of the original data's structure, ensuring that the reconstructed data more accurately reflects the original datasets. The other unit-cell geometries were similarly generated and processed using the same steps as described for the BCC structure, thereby producing a consistent set of training data.

Stiffness matrix calculation

We calculated the stiffness matrix of the generated unit cell data structure in the elastic range using the homogenization method [32], building on the preprocessed data. For constituent material, the Young's modulus and the Poisson's ratio are arbitrarily set to be 2.8GPa and 0.3, respectively, to match the properties of the resin intended for the 3D printing experiments. During the training process, rather than using the entire stiffness matrix, we used the young's modulus in the z -direction, E_z , as the property data for training. E_z was calculated from the stiffness matrix, providing a comprehensive measure of the material's resistance to deformation. Specifically, E_z , represents the axial stiffness in the direction of the z -axis, which is a critical parameter indicating the material's ability to withstand compressive loads along that axis. Various element of the stiffness matrix can be also selected for training depending on the property requirement of the unit cell to be designed. Through this process, we created the randomly generated BCC unit cells and

its stiffness matrix dataset for training the VAE model.

Deep generative models

In this study, we employed deep generative models to generate data with targeted properties. Deep generative models, such as Generative Adversarial Network (GAN) and Variational Autoencoder (VAE), are advanced machine learning frameworks that learn to mimic complex data distributions effectively. GAN excels at generating high-quality data, but their lack of an explicit encoding mechanism makes it difficult to manipulate the latent space for achieving specific properties. In contrast, VAE provides a continuous latent space that can be readily manipulated, making them particularly suitable for generating data with targeted properties. This flexibility and control over the generative process led us to select a VAE for this study. Moreover, handling lattice data represented as point cloud data presents specific challenges, such as the absence of connectivity information and the irregular distribution of data points. By employing a vanilla VAE, we effectively learned well-known lattice data and explored the generation of new data points between existing datasets. This approach allowed us to observe how the VAE could interpolate and create new, meaningful data based on a well-structured latent space.

The VAE is a robust generative machine learning model designed to learn complex data distributions [33]. It consists of an encoder and a decoder and is trained to minimize the loss functions, thereby optimizing the parameters of both the encoder and decoder. As shown in Figure 2(C), we trained a VAE using the generated structure dataset. In the training of the VAE, the point cloud data \mathbf{x} is used as input, which is typically high dimensional. Then, an encoder compresses \mathbf{x} into a lower-dimensional latent space, specifically representing the probability distribution $\mathbf{q}_{\theta}(\mathbf{z}|\mathbf{x})$ of the latent vector \mathbf{z} , where θ are the parameters of the encoder. Typically, the encoder

assumes a normal distribution to effectively represent $q_{\theta}(\mathbf{z}|\mathbf{x})$. Consequently, the encoder outputs two things: a mean vector $\boldsymbol{\mu}$ and a standard deviation vector $\boldsymbol{\sigma}$, representing the parameters of a probability distribution over the latent space. A latent vector \mathbf{z} is sampled from this distribution. The reparameterization trick is employed to sample \mathbf{z} to allow backpropagation through random sampling. The decoder aims to approximate the distribution of \mathbf{x} from the latent vector \mathbf{z} , denoted as $p_{\varphi}(\mathbf{x}|\mathbf{z})$, where φ are the parameters of the decoder. Then, we can generate a new sample $\hat{\mathbf{x}}$ from $p_{\varphi}(\mathbf{x}|\mathbf{z})$. Since data is generated from the latent vector, the decoder serves the role of a generative model. The loss function of VAE is based on the Evidence Lower Bound (ELBO), representing the negative log-likelihood with an added regularization term from the Kullback-Leibler (KL) divergence. Therefore, the loss function is defined to be:

$$\mathcal{L}(\boldsymbol{\theta}, \boldsymbol{\varphi}) = -\mathbf{E}_{\mathbf{z} \sim q_{\theta}(\mathbf{z}|\mathbf{x})} \left[\log \left(p_{\varphi}(\mathbf{x}|\mathbf{z}) \right) \right] + \mathbf{D}_{KL}[(q_{\theta}(\mathbf{x}|\mathbf{z})|p(\mathbf{z}))] \quad (1)$$

The first term from the Equation 1 represents the reconstruction loss. It measures how well the VAE can reconstruct the original input data \mathbf{x} from latent vector \mathbf{z} by comparing \mathbf{x} with its reconstructed data $\hat{\mathbf{x}}$. The second term from the Equation 1 is the KL divergence between the approximate posterior $q_{\theta}(\mathbf{z}|\mathbf{x})$ and the prior distribution $p(\mathbf{z})$ over the latent vector. This term acts as a regularizer, encouraging the distribution inferred by the encoder to be close to the prior. It ensures that the latent space has good properties that allow for generative processes. Without this regularization, training solely on reconstruction loss may not yield a meaningful latent space, potentially impairing the model's generative capabilities.

Property prediction with regressor

Combining the VAE with a regressor, we trained them simultaneously to enable property

prediction using the latent vectors through the regressor [34]. This trained regressor allows for rapid calculation of properties without undergoing complex homogenization methods. Consequently, properties of data generated through the decoder from newly sampled latent vectors could be quickly computed using the regressor. This method enables swift generation of data with targeted properties, demonstrating a significant advancement in efficiency and effectiveness. Additionally, this strategy effectively organizes data with similar properties to cluster together in the latent space.

Loss functions

For the training of the VAE and the regressor, four types of losses are used, as described in Equation 2. As explained in Equation 1, both regularization loss and reconstruction loss are employed in the training of the VAE, and additionally, a contrastive loss and a regression loss are also implemented. Moreover, the regularization loss, regression loss and contrastive loss are each weighted by factors of β , γ and δ , respectively.

$$\mathcal{L} = \mathcal{L}_{reconstruciton} + \beta \times \mathcal{L}_{regularization} + \gamma \times \mathcal{L}_{regression} + \delta \times \mathcal{L}_{contrastive} \quad (2)$$

As previously mentioned, the KL divergence is used as the regularization loss. This component provides a normalization effect, ensuring that the latent space representations align well with the assumed prior distribution. For the reconstruction loss, the Chamfer distance is employed. This metric is particularly effective in assessing how closely the reconstructed point clouds match the original inputs. The Chamfer distance, as defined in Equation 3, sums the nearest point distances between the two sets of points, ensuring that the reconstruction quality of VAE maintains the spatial integrity and distribution of the original data [33].

$$d_{CD}(\mathcal{S}_1, \mathcal{S}_2) = \sum_{x \in \mathcal{S}_1} \min_{x' \in \mathcal{S}_2} \|x - x'\|_2^2 + \sum_{x \in \mathcal{S}_2} \min_{x' \in \mathcal{S}_1} \|x - x'\|_2^2 \quad (3)$$

Additionally, the regression loss is calculated as the mean square error (MSE) between the actual properties of the data and the properties predicted by the regressor. Therefore, through the encoder, a continuous structured latent space is constructed where data with similar shapes are located near each other in the latent space. However, since the objective is to generate data with targeted properties, an additional contrastive loss term is incorporated into the training. This encourages data with similar properties to cluster closer together in the latent space. Manipulating the latent space in this way enables the model to more effectively generate data with the targeted properties.

Contrastive loss

To enhance the model's ability to cluster data based on properties and to generate data with targeted properties, we employed contrastive loss. The contrastive loss works by reducing the distance between similar data points while increasing the distance between dissimilar ones in the latent space. This loss can be formalized as follows:

$$\mathcal{L}_{contrastive} = \frac{1}{n^2} \sum_{i=1}^n \sum_{j=1}^n [S_{ij} \cdot D_{ij}^2 + (1 - S_{ij}) \cdot \max(\mathit{margin} - D_{ij}, \mathbf{0})^2] \quad (4)$$

where n represents the total number of point cloud data points, S_{ij} is the similarity matrix and D_{ij} is the Euclidean distance between the latent vectors \mathbf{z}_i and \mathbf{z}_j [35-37]. The similarity matrix is S_{ij} defined such that $S_{ij} = \mathbf{1}$ if $|\mathbf{y}_i - \mathbf{y}_j| \leq \mathit{threshold}$, indicating similarity, where \mathbf{y}_i and \mathbf{y}_j represents the properties of the respective data. Otherwise, $S_{ij} = \mathbf{0}$ indicates dissimilarity when the property difference exceeds the threshold. Furthermore, the ' margin ' parameter determines the required minimum distance between dissimilar data within the latent space. By training the

VAE with the contrastive loss, the model is optimized to position data with similar properties closer together in the latent space. Furthermore, this approach enables the VAE to learn not only the reconstruction of the data but also the relationships between properties and data, enhancing its overall learning capability. Such an arrangement in the latent space enhances the ability to generate data with targeted properties more effectively.

Generation of BCC unit cell structures with targeted properties

We trained the model on both individual unit cell types and a combined dataset encompassing all types. This section focuses first on results from training with only the BCC unit cell type. We proceeded with training by optimizing key hyperparameters, such as loss function weights and latent dimension, to improve reconstruction accuracy and achieve clustering in the latent space based on both geometric features and E_z values. Here, we demonstrate the generation of new data with targeted E_z values using the optimized latent space of the VAE and regressor. New data were generated through linear interpolation between existing data points in the latent space. First, considering the distances between points in the latent space, we formed a directed graph by connecting k-nearest data points with higher or lower E_z values. We then randomly selected two points as the start and end points. To identify the trend in E_z value changes between these two points, we found the shortest path connecting them. On this path, we aimed to find new latent vectors corresponding to new structure with targeted E_z values.

To demonstrate the interpolation process in detail, consider the following example: Between each pair of neighboring latent vectors on the path, we identified the E_z values of these vectors, denoted as v_1 and v_2 . By scaling these values by a factor of 100 and using all integer values within the range $(100v_1, 100v_2)$. These integer values, when divided by 100, provided the

targeted E_z values. Specifically, we employed targeted E_z values defined as $0.05 \times m$ (where m is an integer). New latent vectors were generated through linear interpolation between existing data points, targeting these targeted E_z values. In this process, a total n latent vectors were generated between each pair of neighboring data points to provide a comprehensive sampling within the latent space. Using the regressor, E_z values for each latent vector were calculated, and those closest to the targeted E_z values were selected.

Figure 3(A), with $k = 5$ and $n = 100$, shows some of the data points in the latent space and the new latent vectors found along the path. The latent space data points used here were a selected subset of the training data, chosen to make the visualization more manageable due to the large number of data points and wide range of E_z values. The black lines and arrows represent the shortest path between randomly selected start and end points, with six existing data points located along the path. The ten green circle marks indicate the new latent vectors chosen to have targeted E_z values between existing data. Figure 3(B) shows the E_z values of the newly generated latent vectors, showing that, except for the highest targeted value, the new latent vectors closely match the targeted values. The discrepancy observed at the highest targeted value can be attributed to the relatively fewer training data points with high E_z values, resulting in a less structured latent space in those regions. From these new latent vectors, we used the decoder to generate new data and computed their parameters. The E_z values calculated using the homogenization method from these newly generated data points are also shown in Figure 3(B), demonstrating an R^2 value of 0.9867 when compared to the values predicted by the regressor. The observed discrepancies can be explained by several factors. First, the point cloud data are irregularly arranged, leading to potential errors in the calculation of data parameters. Additionally, the process of voxelization required for applying the homogenization method can introduce further inaccuracies. Figure 3(C) illustrates

the new data generated from these latent vectors using the decoder, which were then scaled up and mirrored to form a BCC structural configuration. The Figure 3(C) also shows the continuous transformation in shape corresponding to changes in the three data parameters from low to high E_z values. Detailed information on each parameter and the calculated E_z values for each progression are thoroughly presented in Table 1. As E_z increases, width and height generally decrease while the strut radius increases. Particularly, during interpolation between the final pairs of existing data on the path, width and height exhibit only minor fluctuations without significant changes, whereas the strut radius increases substantially. Notably, the strut radius of the original data ranges between 1 and 3, but the newly generated data features strut radius exceeding 3. By choosing different start and end points, we can discover new paths within the latent space, leading to the generation of diverse data shapes. This flexibility to explore various trajectories in the latent space underscores the model's potential for creating a wide range of structural forms based on intricate interrelationships between E_z values and data parameters. Increasing the value of k or n could lead to more precise generation. Furthermore, data corresponding to arbitrary E_z values could also be generated.

To create actual microlattice structures from these newly generated point cloud data, it is necessary to construct solid models. In the case of BCC structures, 3D models were created using the data parameters extracted from the point cloud data. Figure 3(D) presents the 3D models of the unit cells created from each point cloud data, which are then stacked into $5 \times 5 \times 5$ lattice. Furthermore, To validate the mechanical properties of the generated lattice structures, we fabricated samples via stereolithography and subjected them to uniaxial compression along the z-axis. Multiple samples of each configuration were fabricated, and tests were performed at varying strain rates to obtain reliable stress-strain curves, as shown in Figure 3(E). The Young's modulus

was determined from the slope of the stress-strain curve within the elastic region. The experimentally obtained relative Young's modulus values were compared with those predicted by the regressor, which were also normalized by the Young's modulus of the constituent material, Figure 3(F) presents the comparison, demonstrating that the relative Young's modulus values from the actual printed samples closely matched the values predicted by the regressor, with a discrepancy of 26.05%. This discrepancy can be attributed to the newly generated point cloud data, which, while generally exhibiting a BCC structure, show irregular and random point distributions at the edges upon closer inspection. This irregularity complicates the precise definition of data parameters, leading to the observed discrepancies. Despite this, the result demonstrates that the newly generated BCC structures accurately achieve the targeted E_z values.

Extension to additional unit cell structures

In this section, we extend the present method to a variety of unit cell structures. The adaptability of this method is exemplified in Figures 4(A) and 4(B), which respectively represents the cubic and octahedron structures. The data from each unit cell were used to train the VAE and regressor, and new structures with targeted properties were generated using the same linear interpolation process. The cubic and octahedron structures, unlike the BCC structure, have three parameters for strut radius. Despite the increase in the number of data parameters, clustering was effectively achieved based on E_z values in the latent space, and latent vectors corresponding to targeted E_z values were successfully generated. Unlike the BCC structure, the range of E_z values were larger, so data was generated using targeted E_z values set as $0.05 \times m$ (where m is an integer) between the existing data points. Here too, to facilitate smooth interpolation and ensure efficient and targeted generation of the necessary structures, only a subset of the data was used due

to the large quantity of data. Figures 4(A) and 4(B) also illustrate the new data generated from targeted E_z values along the path within the subset of the latent space between existing data points. The E_z values were calculated using both the regressor and the homogenization method, showing R^2 values of 0.9894 and 0.9547, respectively. Additionally, these figures demonstrate how the shapes of the structures change between the existing data points when new data is generated using the decoder. The data parameters for each newly generated point cloud dataset are detailed in Tables 2 and 3. Figures 4(A) and 4(B) present the 3D models of unit cells created from the subset of newly generated point cloud data, which are then stacked to form lattice structures of comparable dimensions. It is important to note that we have not yet optimized the hyperparameters for these specific structures, which may account for the observed decrease in reconstruction quality. Despite this, as E_z increases, the overall size decreases in cubic structures and increases in octahedron structures, while the strut radius generally increases, resulting in the generation of new data corresponding to the targeted E_z values. Given the multiple data parameters involved, there is likely a more intricate relationship between E_z and these parameters. Similar to the BCC structures, the actual properties of the newly generated data were validated by fabricating lattice structures and conducting compression tests to compare with the regressor values. Then, Figures 4(A) and 4(B) display the fabricated samples and the corresponding compression test results for each structure. Upon comparing the relative Young's modulus, discrepancies of 17.77% and 9.42% were observed, respectively. It is anticipated that, with further optimization of the hyperparameters tailored to these specific structures, significant improvements in reconstruction quality can be achieved. Although there has been an increase in both the number of points in the point cloud data and the data parameters, this variation aligns with the targeted E_z values. Expanding upon this, the successful adaptation of our method to these complex unit cell structures not only validates its

versatility but also its precision in generating and predicting specific structural properties. The transition to more intricate cell designs, such as the cubic and octahedron structures, showcases the potential of this approach in a broader range of applications.

Simultaneous Training on Diverse Unit Cell Types

In previous sections, we focused on training the VAE model with only one type of unit cell design at a time, generating unit cell designs corresponding to that specific type. However, here we trained the model simultaneously on various types of unit cells. The six different types of unit cell point cloud data trained are presented in Figure 2(A), and correspondingly, the PCA results of latent space in Figure 5(A) show six distinct clusters, representing the distribution according to E_z values and variation based on data type. Each cluster corresponds to a different structural class from the six unit cell types we used. Despite training on various structural types simultaneously, each structure is effectively reconstructed, closely resembling the original data. This indicates the model's effectiveness in maintaining the integrity of diverse structural types during the reconstruction process. Within each cluster, we observed effective clustering according to E_z values. However, when considering the overall latent space, a clear trend is not apparent. Thus, while it is feasible to generate new data corresponding to targeted E_z values within individual clusters, discerning the distribution of data between clusters remains challenging. To address this, we generated new data both within the clusters and in the regions between clusters to better understand the overall data distribution in the latent space.

Initially, we focused on generating new data within the clusters, similar to our previous approach with a single structure. In this approach, we created a directed graph, identified the shortest path between two points, and interpolated new latent vectors along this path based on

targeted E_z values. The right side of Figure 5(A) illustrates this process for each structure, depicting the newly generated latent vectors along the path and the corresponding data produced via the decoder. Notably, the newly generated data conform to the structural characteristics of their respective clusters, indicating that the latent space effectively clusters data by structural type. This finding confirms that the latent space is well-organized according to structural types, allowing for accurate generation and interpolation of new data points within each cluster.

Following the exploration within individual clusters, we proceeded to generate data in the transitional regions between clusters to further explore the latent space and understand the distribution and potential transitions between various structural types. Given the difficulty in forming directed graphs and identifying the shortest paths between clusters as we did within clusters, we adopted a different approach for these transitional regions. Specifically, we identified data points with certain E_z values within each cluster and connected these points to neighboring clusters. This process created loops, as shown in the Figure 5(B). By performing linear interpolation between neighboring data points within these loops, we generated new data and observed the changes in E_z values. In detail, we selected E_z data points with a value of 0.050 from each cluster and generated new data points between existing data points. This involved linear interpolation between existing latent vectors to create new latent vectors, calculating their E_z values using the regressor, and generating new point cloud data through the decoder. The newly generated data points and their corresponding E_z values are shown in Figure 5(C), where one representative example from the interpolations is displayed along with its predicted properties. While the E_z values are not exactly 0.05, they are mostly close to this value. Additionally, Figure 5(D) provides a more detailed view of the interpolated shapes, illustrating how the newly generated forms exhibit smooth transitions in topology between the original data points, resulting in novel

configurations not present in the initial dataset. For example, in the linear interpolation between bcc data (A) and cubic data (B), the generated data illustrate how the bcc structure transitions to a cubic structure. This transformation is characterized by the creation of empty spaces in the center and the spreading of struts towards the corners, resulting in a cubic configuration.

To validate the properties of these newly generated data, we encountered a challenge because, unlike previous cases, these data presented new forms not seen in the original dataset, making it impossible to calculate data parameters due to the lack of predefined shapes. Therefore, we needed a method to convert these novel point cloud data into a format suitable for manufacturing, as point cloud data, while useful for visualization, is not directly usable for additive manufacturing, which requires surface or volume data for actual printing. One effective method for converting point cloud data into surface mesh suitable for manufacturing is the ball-pivoting algorithm. This technique is used to create surface mesh from point cloud data by literally ‘pivoting’ a ball around the points to identify nearby points to form surfaces. Figure 6(A) demonstrates how this algorithm works on a 2D point cloud. For a 3D point cloud, the ball touches three points to form a triangular mesh and generate surface data. Due to its operational principle, the ball-pivoting algorithm is most effective when every point in the point cloud is uniformly distributed. However, as shown in the steps in Figure 6(A), the output point cloud of our model is randomly distributed, resulting in insufficient surface reconstruction quality for manufacturing. To address this issue, the entire structure of the point cloud is divided into voxels, and each point is relocated to the center of the nearest voxel. This process evenly distributes all points, as shown in Figure 6(A), but may lead to some structures being missed or distorted due to relocation. Compensation is achieved by using the moving average method, which references surrounding points of each voxel center and includes this center point in the data if the number of surrounding points exceeds a certain threshold.

The adjusted, evenly distributed point cloud and the ball-pivoting surface reconstruction result are shown as steps in Figure 6(A). This figure illustrates that this surface reconstruction method can be applied even in complex geometries like the interpolated structure between octet-truss and fluorite. Through this process, we converted the newly generated data obtained by interpolation between structures of different types into 3D surface models. Using these models, we fabricated lattice structures and subjected them to compression tests to calculate the relative Young's modulus, comparing the results with the values predicted by the regressor. This process followed the same steps as described earlier. Figures 6(B) and 6(c) display the fabricated samples from each point cloud data and the corresponding compression test results. On average, a discrepancy of 11.56% was observed, which can be attributed to the complexities involved in the surface reconstruction. Nonetheless, these newly generated data, exhibiting forms not seen in the original dataset, showed a strong agreement between the experimental values and the regressor's predictions.

This observation highlights the model's ability to generate intermediate structures with unique properties. The smooth transitions in topology illustrated in Figure 6(D) further underscore the model's capacity to create novel configurations by bridging different structural types. Consequently, we next focused on examining how E_z values distribute in the regions of the latent space that lie between these clusters, particularly in areas lacking original data points. By rapidly calculating and analyzing these distributions using the regressor, we can potentially generate new data corresponding to targeted E_z values based on these distributions. This approach might enable us to create various new structural forms that were not evident in the original training data. This development suggests that our model could be capable of creating a wider variety of structures than those present in our current dataset, opening possibilities for generating new and unique forms.

Discussion

The present study aimed to design unit cells that form metamaterials with various shapes possessing targeted properties, addressing the challenges of traditional material design processes characterized by extensive computational efforts and complex geometric modeling. By integrating deep generative models, specifically a Variational Autoencoder (VAE), along with a regressor, enabled the efficient design and rapid prototyping of microlattice structures. We trained a VAE and a regressor using diverse 3D point cloud data and stiffness matrix for properties, enabling the design of geometric parameters of unit cells with specific mechanical properties through linear interpolation. Unlike graph-based methods, using point cloud data allowed for the easy creation of complex structures without the need for connecting points. Furthermore, instead of using complex calculations through the homogenization method, employing the regressor enabled rapid calculation of new data properties. As a result, we were able to design various unit cell geometries with targeted properties, such as BCC, octet-truss, and kelvin foam, and also create new forms of unit cells not previously observed. Additionally, the point cloud data was converted into 3D mesh models for fabrication using 3D printing, and the resulting structures demonstrated E_z values closely matching those predicted by the regressor.

Although this study trained the model with only strut-based data, the adaptability of point clouds to represent complex surfaces suggests that training with surface-type data could broaden the scope of structural designs achievable by this method. Furthermore, expanding the property data beyond the E_z value of the stiffness matrix to include the entire matrix, as well as other properties such as density or thermal transport, could enable the generation of data with diverse targeted physical properties. Training on multiple classes simultaneously, rather than single classes separately, might also lead to the generation of unique structures not previously seen in

the existing unit cell library.

In addition, the current study utilizes a vanilla VAE as the training model. Advances in VAE research suggest that integrating more sophisticated architectures could enhance training efficiency, stability, and reconstruction quality, improving the model's capability to generate high-fidelity designs. Furthermore, the present training model's capability to establish a one-to-many functional relationship between E_z values and data parameters could enable the identification of data parameter sets corresponding to specific E_z values, potentially enhancing the model's precision and applicability.

This work establishes a foundation for designing microlattice structures with targeted mechanical properties, expanding the possibilities for creating advanced mechanical metamaterials. The approach not only enhances the design process for complex architectures but also enables new forms that transcend traditional design constraints. By expanding this method to other physical properties and integrating it with additive manufacturing, we anticipate applications in diverse fields opening avenues for innovation in both industrial and research settings.

Materials and Methods

Model architecture and training

The VAE architecture used in this study consists of an encoder with five 1D convolutional layers, efficiently compressing the input data into a meaningful latent space. On the other hand, the decoder is simpler with two layers to prevent overfitting. In both the encoder and decoder, each layer employs the ReLU activation function, enabling the model to effectively learn non-linear patterns in the data [38]. Additionally, batch normalization is also used in the encoder for fast and stable learning [39]. Point cloud data is unique in that changing the order of points in the input

does not change what it represents. Therefore, it is important that the output data stays the same even if the order of the input points changes. To achieve this invariance to point order, we have incorporated a max-pooling function at the end of the encoder. It ensures that the training process is independent of the order of points in the input data. Subsequently, two fully connected neural networks are employed to obtain the mean and variance of the latent vector. As previously explained, we utilize the reparameterization trick to sample the latent variable \mathbf{z} from the obtained mean and variance. The sampled \mathbf{z} is then processed through the decoder and the decoder reconstructs the output data to have the same number of points as the original input data. The previously generated dataset comprises 10,000 data points for each data type, split into training, testing, and validation sets in an 8:1:1 ratio. Training typically involves 500 epochs by default, but we applied an early stopping technique to prevent overfitting [40]. Simultaneously with the VAE, the regressor is also trained to predict the E_z values from the latent vectors of each data. The regressor consists of four fully connected layers. The regressor only uses the mean value of latent vector given by the encoder as its input. The VAE is trained with a learning rate of 10^{-6} , while the regressor is trained with a learning rate of 10^{-5} . All model training and testing were conducted on a workstation equipped with an NVIDIA GeForce RTX 3090 GPU and 256GB of RAM.

Fabrication of generated structures

To validate the properties of these newly generated structures, we fabricated the lattice structures using a stereolithography (SLA) printer (FormLabs Form3L) with Photocurable Resin (FormLabs Clear V4). The lattice structures were formed by stacking the unit cells into $5 \times 5 \times 5$ configurations, with a layer thickness of 100 μm . After printing, the structures were washed in isopropyl alcohol, then fully cured under UV light for 1 hour as post processing, to ensure complete

polymerization.

Mechanical testing

The fabricated samples were subjected to compression tests by applying load along the z-axis direction with customized mechanical tester. The tests were conducted at a compression rate of 5 mm/min within a strain range of 4~6%, and each sample was tested more than five times to ensure reliability of experimental results. The Young's modulus of sample was determined from the stress-strain curve result by calculating the slope in the elastic region using linear regression method.

References

- [1] X. Zheng *et al.*, "Ultralight, ultrastiff mechanical metamaterials," *Science*, vol. 344, no. 6190, pp. 1373-1377, 2014.
- [2] X. Chen *et al.*, "Light-weight shell-lattice metamaterials for mechanical shock absorption," *International Journal of Mechanical Sciences*, vol. 169, p. 105288, 2020.
- [3] Z. G. Nicolaou and A. E. Motter, "Mechanical metamaterials with negative compressibility transitions," *Nature materials*, vol. 11, no. 7, pp. 608-613, 2012.
- [4] H. Wang, Y. Zhang, W. Lin, and Q.-H. Qin, "A novel two-dimensional mechanical metamaterial with negative Poisson's ratio," *Computational Materials Science*, vol. 171, p. 109232, 2020.

- [5] C. W. Li *et al.*, "Structural Relationship between Negative Thermal Expansion and Quartic Anharmonicity of Cubic ScF₃," *Physical review letters*, vol. 107, no. 19, p. 195504, 2011.
- [6] A. Vyatskikh, S. Delalande, A. Kudo, X. Zhang, C. M. Portela, and J. R. Greer, "Additive manufacturing of 3D nano-architected metals," *Nature communications*, vol. 9, no. 1, p. 593, 2018.
- [7] P. Li, F. Yang, Y. Bian, S. Zhang, and L. Wang, "Designable mechanical properties of modified body-centered cubic lattice materials," *Composite Structures*, vol. 317, p. 117060, 2023.
- [8] J. Bauer, A. Schroer, R. Schwaiger, and O. Kraft, "Approaching theoretical strength in glassy carbon nanolattices," *Nature materials*, vol. 15, no. 4, pp. 438-443, 2016.
- [9] H. A. Eschenauer and N. Olhoff, "Topology optimization of continuum structures: a review," *Appl. Mech. Rev.*, vol. 54, no. 4, pp. 331-390, 2001.
- [10] Y. Zheng, Y. Wang, X. Lu, Z. Liao, and J. Qu, "Evolutionary topology optimization for mechanical metamaterials with auxetic property," *International Journal of Mechanical Sciences*, vol. 179, p. 105638, 2020.
- [11] J. Liu, V. Nguyen-Van, B. Panda, K. Fox, A. du Plessis, and P. Tran, "Additive manufacturing of sustainable construction materials and form-finding structures: a review on recent progresses," *3D Printing and Additive Manufacturing*, vol. 9, no. 1, pp. 12-34, 2022.
- [12] Y. Mao, Q. He, and X. Zhao, "Designing complex architected materials with generative adversarial networks," *Science advances*, vol. 6, no. 17, p. eaaz4169, 2020.

- [13] L. Wang, Y.-C. Chan, F. Ahmed, Z. Liu, P. Zhu, and W. Chen, "Deep generative modeling for mechanistic-based learning and design of metamaterial systems," *Computer Methods in Applied Mechanics and Engineering*, vol. 372, p. 113377, 2020.
- [14] S. Lee, Z. Zhang, and G. X. Gu, "Generative machine learning algorithm for lattice structures with superior mechanical properties," *Materials Horizons*, vol. 9, no. 3, pp. 952-960, 2022.
- [15] S. Luan, E. Chen, J. John, and S. Gaitanaros, "A data-driven framework for structure-property correlation in ordered and disordered cellular metamaterials," *Science Advances*, vol. 9, no. 41, p. eadi1453, 2023.
- [16] O. Eren, N. Yüksel, H. R. Börklü, H. K. Sezer, and O. E. Canyurt, "Deep learning-enabled design for tailored mechanical properties of SLM-manufactured metallic lattice structures," *Engineering Applications of Artificial Intelligence*, vol. 130, p. 107685, 2024.
- [17] C. J. Court, B. Yildirim, A. Jain, and J. M. Cole, "3-D inorganic crystal structure generation and property prediction via representation learning," *Journal of Chemical Information and Modeling*, vol. 60, no. 10, pp. 4518-4535, 2020.
- [18] X. Zheng, T.-T. Chen, X. Jiang, M. Naito, and I. Watanabe, "Deep-learning-based inverse design of three-dimensional architected cellular materials with the target porosity and stiffness using voxelized Voronoi lattices," *Science and Technology of Advanced Materials*, vol. 24, no. 1, p. 2157682, 2023.
- [19] L. Makatura *et al.*, "Procedural metamaterials: A unified procedural graph for metamaterial design," *ACM Transactions on Graphics*, vol. 42, no. 5, pp. 1-19, 2023.

- [20] Y. Li *et al.*, "Generalized deep 3D shape prior via part-discretized diffusion process," in *Proceedings of the IEEE/CVF Conference on Computer Vision and Pattern Recognition*, 2023, pp. 16784-16794.
- [21] S. Bonfanti, S. Hiemer, R. Zulkarnain, R. Guerra, M. Zaiser, and S. Zapperi, "Computational design of mechanical metamaterials," *Nature Computational Science*, vol. 4, no. 8, pp. 574-583, 2024.
- [22] D. P. Kingma, "Auto-encoding variational bayes," *arXiv preprint arXiv:1312.6114*, 2013.
- [23] Y. Zhou and O. Tuzel, "Voxelnet: End-to-end learning for point cloud based 3d object detection," in *Proceedings of the IEEE conference on computer vision and pattern recognition*, 2018, pp. 4490-4499.
- [24] Ö. Çiçek, A. Abdulkadir, S. S. Lienkamp, T. Brox, and O. Ronneberger, "3D U-Net: learning dense volumetric segmentation from sparse annotation," in *Medical Image Computing and Computer-Assisted Intervention—MICCAI 2016: 19th International Conference, Athens, Greece, October 17-21, 2016, Proceedings, Part II 19*, 2016: Springer, pp. 424-432.
- [25] Y. Wang, Y. Sun, Z. Liu, S. E. Sarma, M. M. Bronstein, and J. M. Solomon, "Dynamic graph cnn for learning on point clouds," *ACM Transactions on Graphics (tog)*, vol. 38, no. 5, pp. 1-12, 2019.
- [26] P. Velickovic, G. Cucurull, A. Casanova, A. Romero, P. Lio, and Y. Bengio, "Graph attention networks," *stat*, vol. 1050, no. 20, pp. 10-48550, 2017.
- [27] R. Q. Charles, H. Su, M. Kaichun, and L. J. Guibas, "PointNet: Deep learning on point sets for 3D classification and segmentation," in *2017 IEEE conference on computer vision and pattern recognition (CVPR)*, 2017: IEEE, pp. 77-85.

- [28] Z. Han, X. Wang, Y.-S. Liu, and M. Zwicker, "Multi-angle point cloud-VAE: Unsupervised feature learning for 3D point clouds from multiple angles by joint self-reconstruction and half-to-half prediction," in *2019 IEEE/CVF International Conference on Computer Vision (ICCV)*, 2019: IEEE, pp. 10441-10450.
- [29] A.-C. Cheng, X. Li, S. Liu, M. Sun, and M.-H. Yang, "Autoregressive 3d shape generation via canonical mapping," in *European Conference on Computer Vision*, 2022: Springer, pp. 89-104.
- [30] W. Xiao, Z. Fan, and Q. Liu, "Point Cloud Generation via Variational Auto-encoder."
- [31] X. Yang, G. Lin, Z. Chen, and L. Zhou, "Neural vector fields: Implicit representation by explicit learning," in *Proceedings of the IEEE/CVF Conference on Computer Vision and Pattern Recognition*, 2023, pp. 16727-16738.
- [32] G. Dong, Y. Tang, and Y. F. Zhao, "A 149 line homogenization code for three-dimensional cellular materials written in matlab," *Journal of Engineering Materials and Technology*, vol. 141, no. 1, p. 011005, 2019.
- [33] H. Fan, H. Su, and L. J. Guibas, "A point set generation network for 3d object reconstruction from a single image," in *Proceedings of the IEEE conference on computer vision and pattern recognition*, 2017, pp. 605-613.
- [34] R. Tibshirani, "Regression shrinkage and selection via the lasso," *Journal of the Royal Statistical Society Series B: Statistical Methodology*, vol. 58, no. 1, pp. 267-288, 1996.
- [35] Y. Li, P. Hu, Z. Liu, D. Peng, J. T. Zhou, and X. Peng, "Contrastive clustering," in *Proceedings of the AAAI conference on artificial intelligence*, 2021, vol. 35, no. 10, pp. 8547-8555.

- [36] R. Hadsell, S. Chopra, and Y. LeCun, "Dimensionality reduction by learning an invariant mapping," in *2006 IEEE computer society conference on computer vision and pattern recognition (CVPR'06)*, 2006, vol. 2: IEEE, pp. 1735-1742.
- [37] A. v. d. Oord, Y. Li, and O. Vinyals, "Representation learning with contrastive predictive coding," *arXiv preprint arXiv:1807.03748*, 2018.
- [38] X. Glorot, A. Bordes, and Y. Bengio, "Deep sparse rectifier neural networks," in *Proceedings of the fourteenth international conference on artificial intelligence and statistics*, 2011: JMLR Workshop and Conference Proceedings, pp. 315-323.
- [39] S. Ioffe, "Batch normalization: Accelerating deep network training by reducing internal covariate shift," *arXiv preprint arXiv:1502.03167*, 2015.
- [40] L. Prechelt, "Early stopping-but when?," in *Neural Networks: Tricks of the trade*: Springer, 2002, pp. 55-69.

Figures and Tables

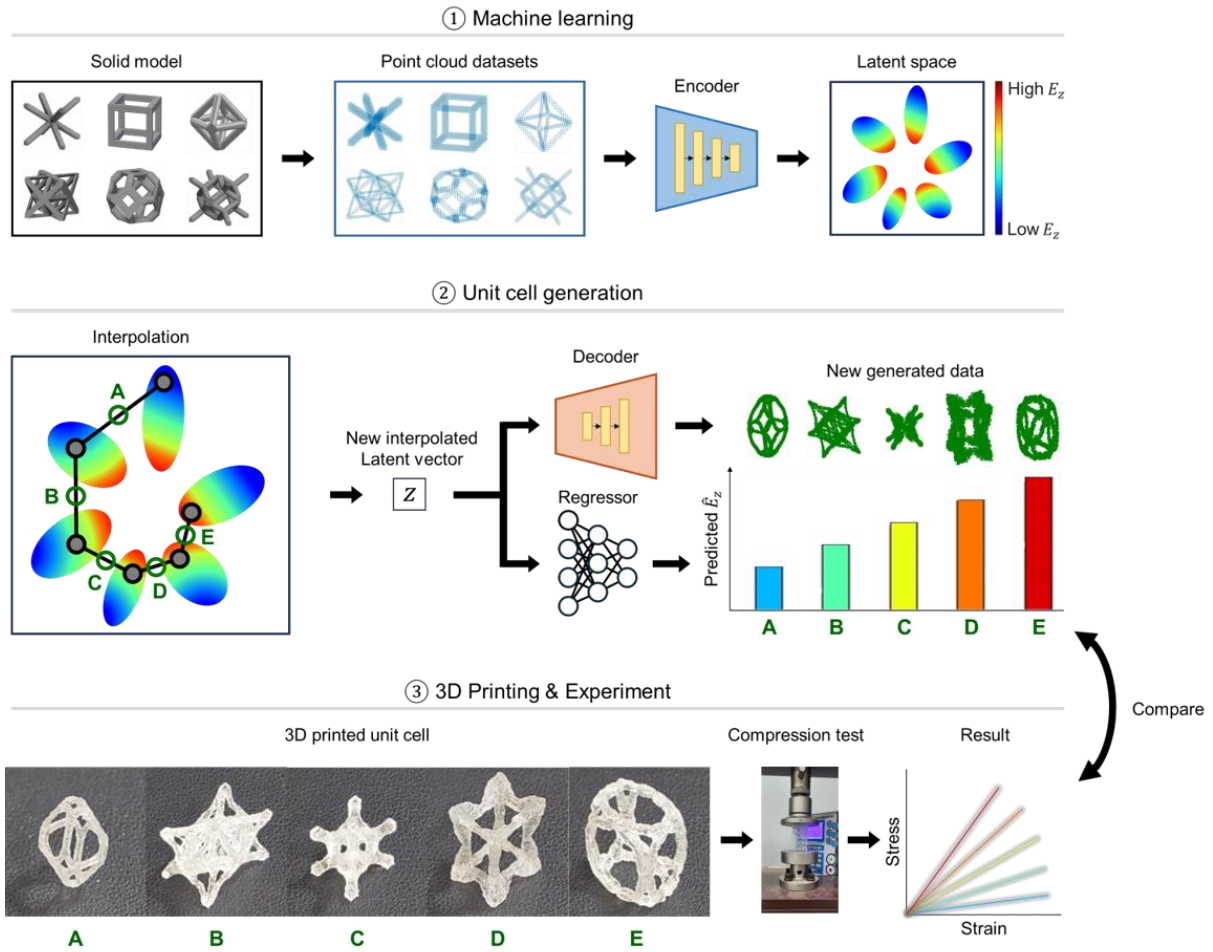


Figure 1. Overview of design strategy and analysis of 3D mechanical metamaterials using point-cloud-based deep generative networks

(A)

	BCC	Cubic	Octahedron	Octet-truss	Kelvin foam	Fluorite
Solid model						
Point cloud model						
Training data						

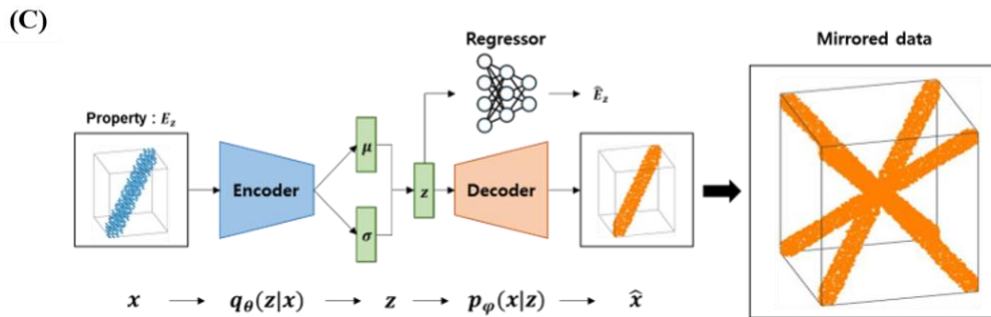
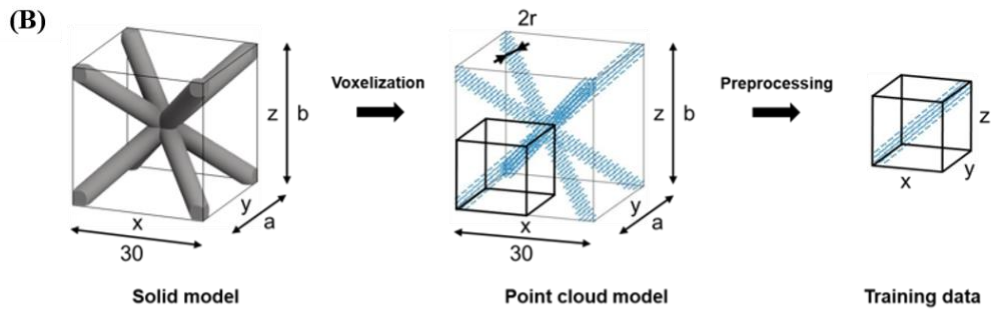


Figure 2. Different types of microlattice structures and data processing and training. (A) Solid model and point cloud data of six different unit cells (B) The generation process and preprocessing of training data. Random values are assigned to a , b , and r to generate body-centered cubic (BCC) data and followed by the preprocessing step to create training data. (C) The schematic architecture of the VAE, along with the mirrored data derived from the output point cloud.

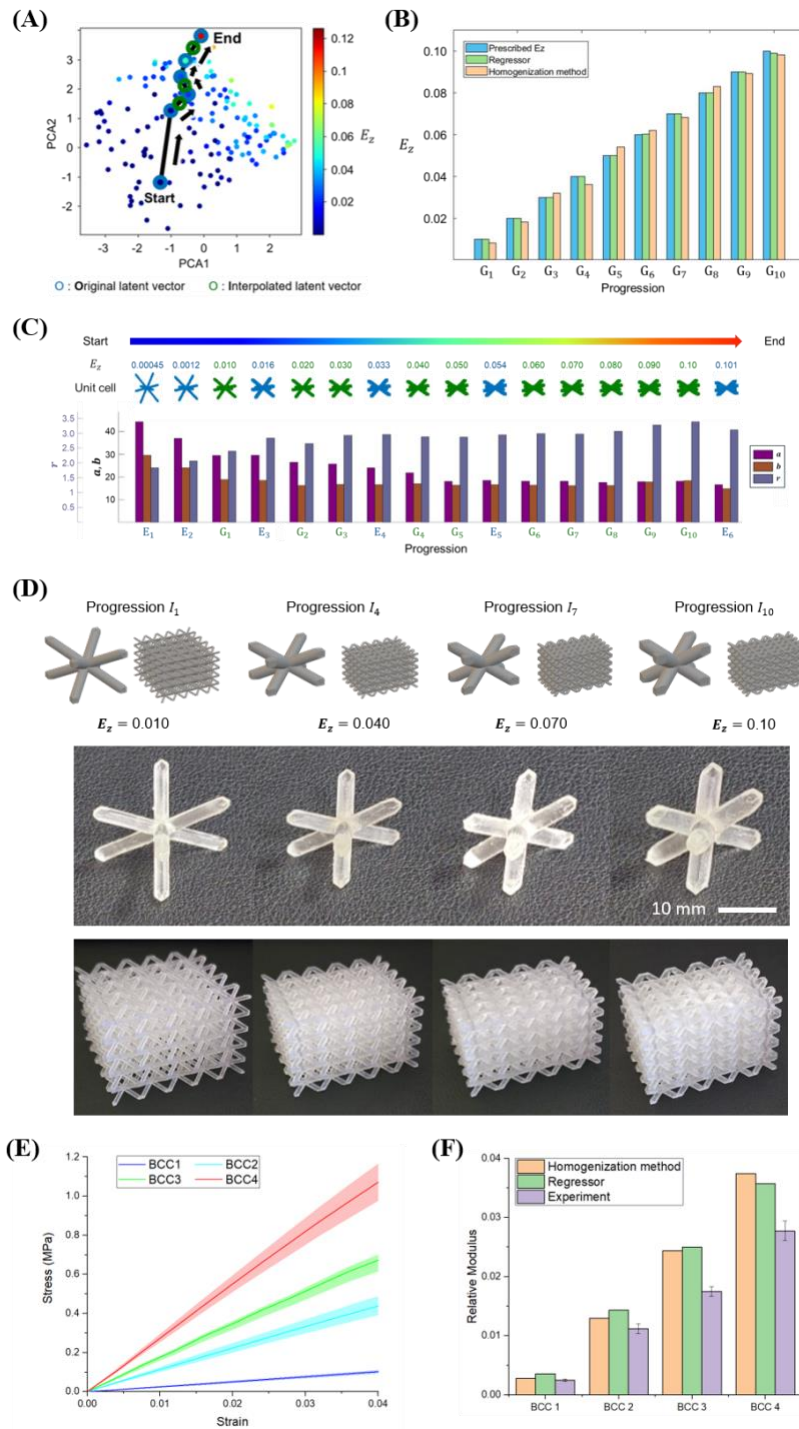


Figure 3. The generation process for new BCC structures with prescribed E_z values. (A)

The directed graph constructed in the subset of latent space with shortest path. The existing data

with blue markers and the new latent vectors generated through linear interpolation with green markers. **(B)** The E_z values of the newly generated data calculated through the regressor and homogenization method. **(C)** The blue original data and the green new data generated from the new latent vectors through the decoder and the variation of the three data parameters in each data. **(D)** The 3D models of unit cells created from the three data parameters calculated from the subset of the newly generated BCC point cloud data, and the lattice structures formed by stacking these unit cells in $5 \times 5 \times 5$ configurations, including those fabricated through 3D printing. The scale bar at the top right corresponds to 10 mm. **(E)** The stress-strain curves of each lattice obtained from compression tests. **(F)** Comparison of the relative Young's modulus values calculated by the homogenization method, predicted by the regressor, and obtained from compression tests.

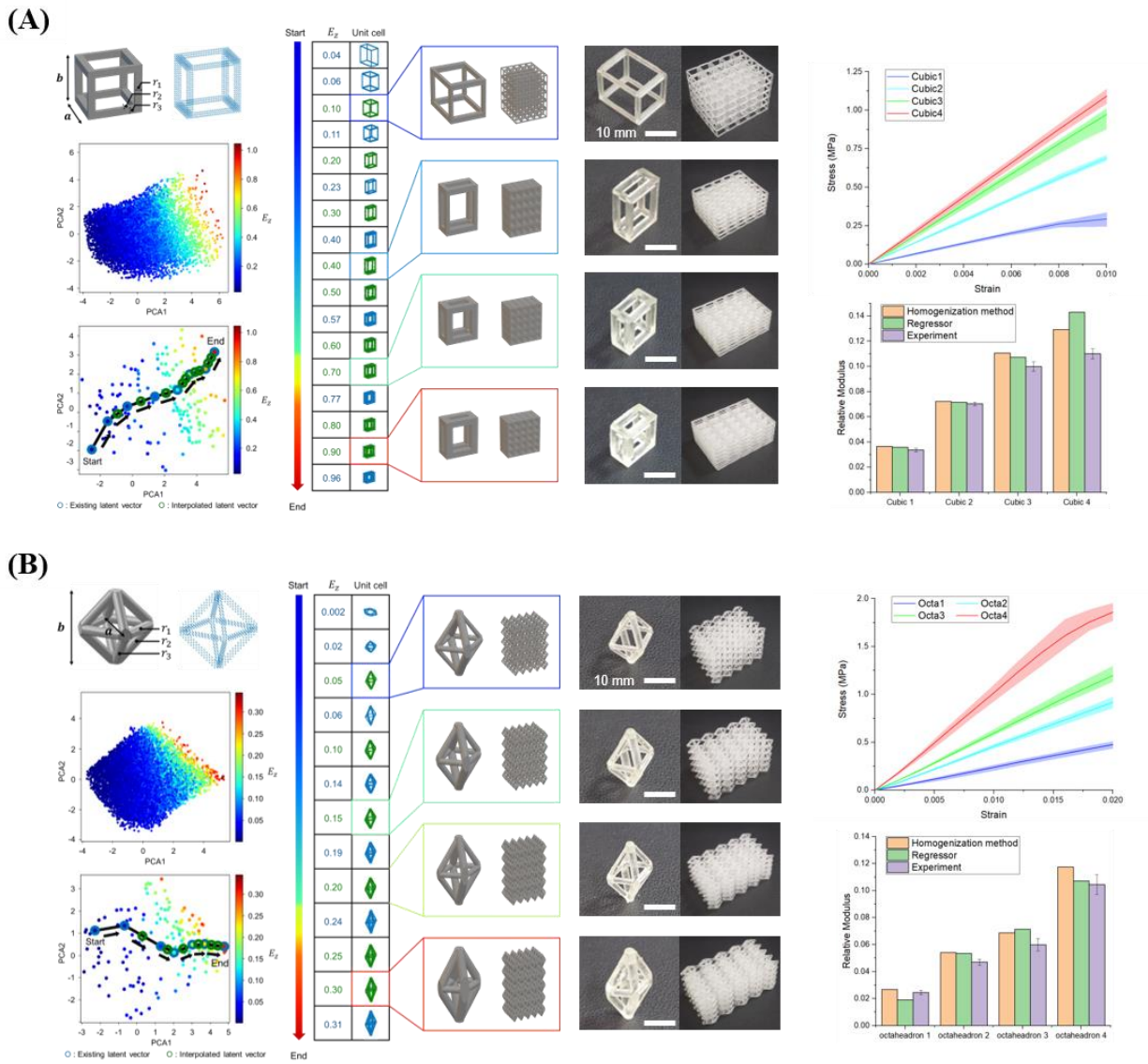


Figure 4. The generation process for new structures with prescribed E_z values, following the methodology applied to the BCC structures: (A) Cubic (B) Octahedron.

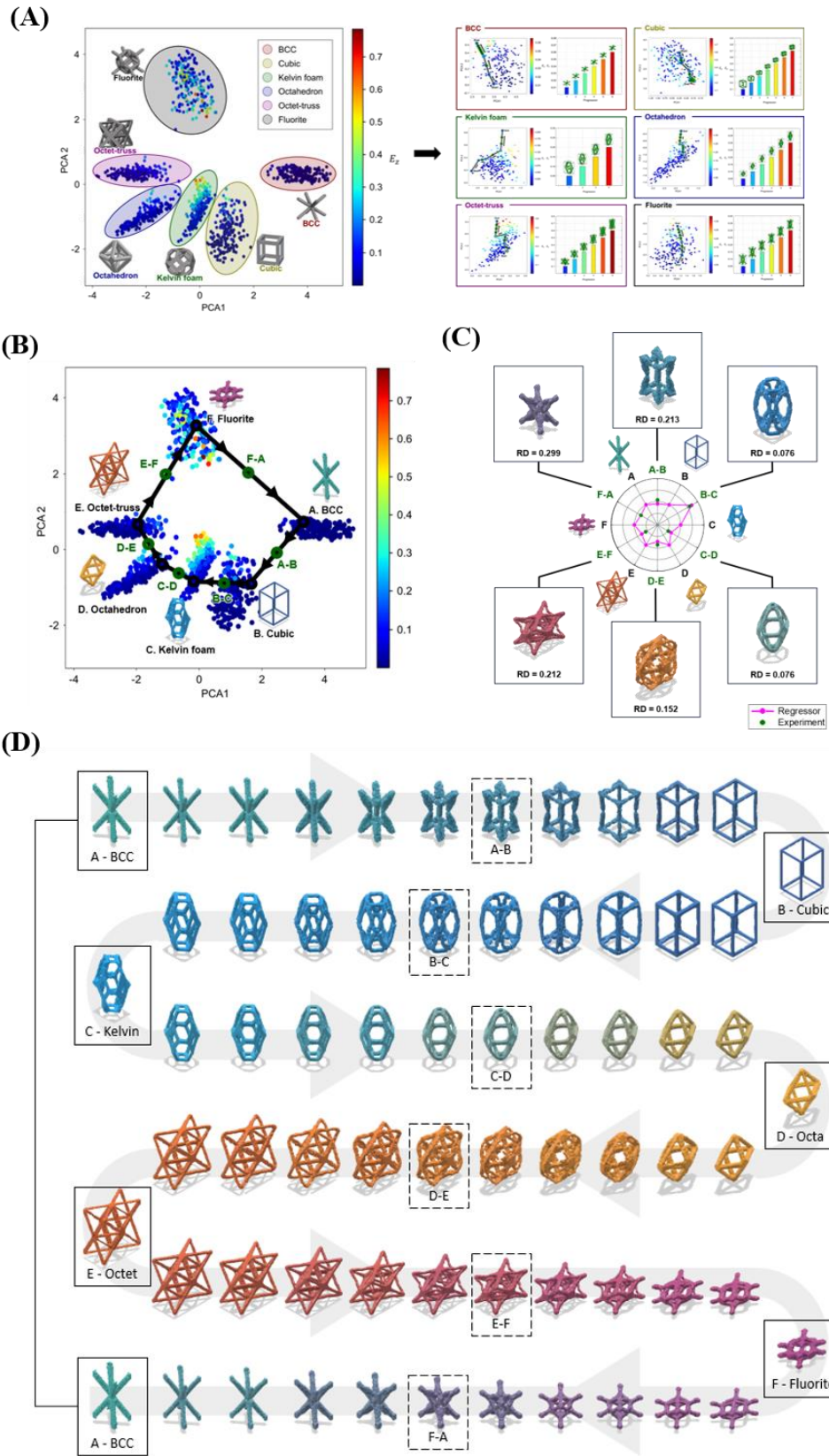


Figure 5. The results of simultaneous training of diverse structural types. (A) The distribution in the PCA results of latent space. The right side illustrates interpolation within each cluster of structures. Green new latent vectors generated through interpolation based on prescribed E_z values, with corresponding unit cell structures generated through the decoder. (B) Data points with E_z values of 0.050 and their connection to form loops between adjacent clusters. Green marks indicate interpolation data points within the clusters. (C) The changes in E_z values for existing data points and newly generated interpolation data points between each pair of existing data points, shown in radar chart. (D) The transition process between selected data points, with 10 steps of newly generated interpolation data between each adjacent lattice.

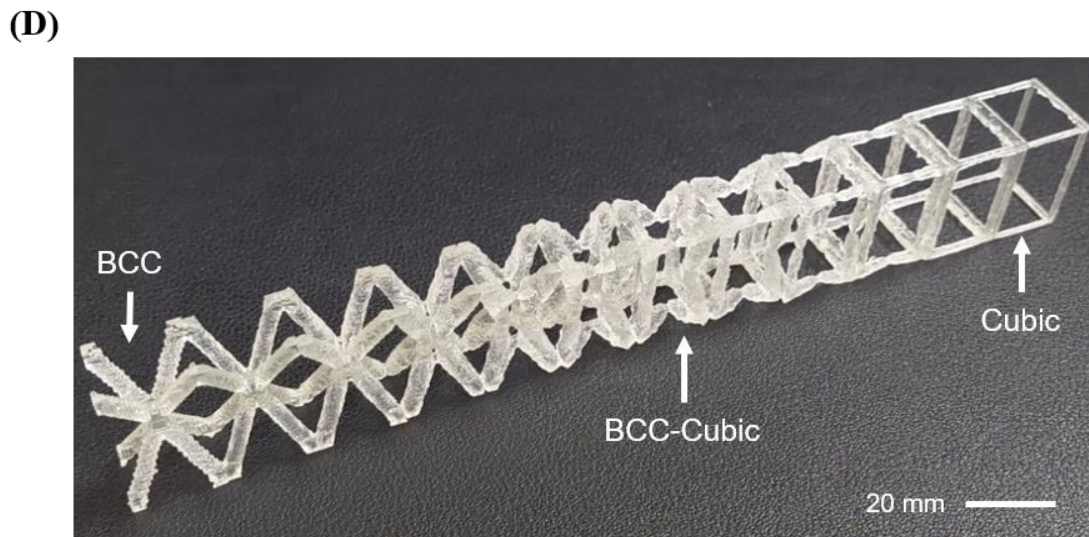
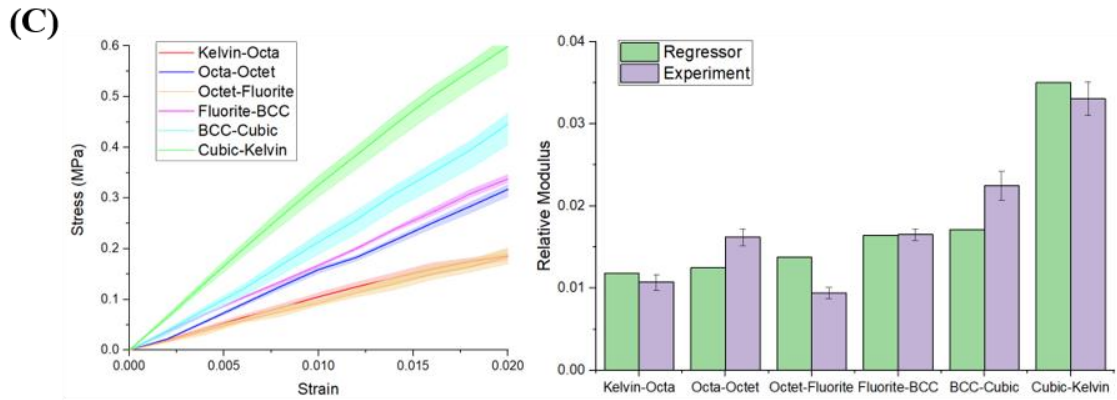
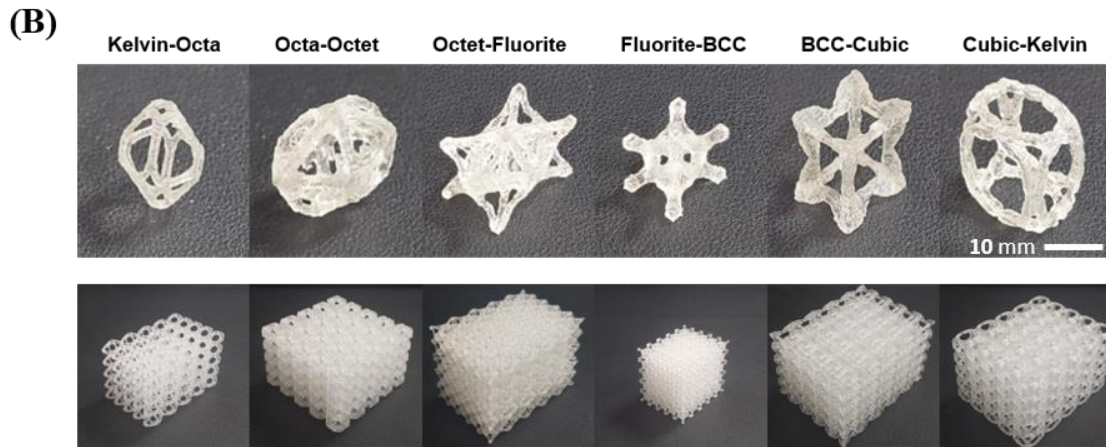
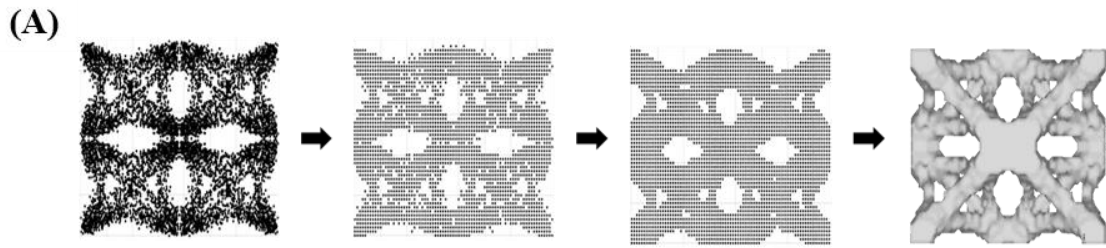


Figure 6. Fabrication and mechanical testing of lattice structures with interpolated unit cells.

(A) Surface reconstruction of newly generated point cloud data from the interpolated structure between octet-truss and fluorite lattice, including evenly spaced point clouds, adjustment using the moving average method, and the final surface reconstruction. (B) Lattice structures fabricated through 3D printing and the scale bar at the bottom right corresponds to 10 mm. (C) Stress-strain curves obtained from compression tests of each lattice, along with a comparison of relative Young's modulus values predicted by the regressor and measured experimentally. (D) Lattice structures fabricated through 3D printing, using transforming unit cell shapes between BCC and cubic structures, all connected in a single line.

Table 1. The three data parameters width (a), height (b), strut radius (r) and E_z calculated from the newly generated BCC point cloud data

Progression	Width (a)	Height (b)	Strut radius (r)	E_z (Regressor)	E_z (Homogenization)
1	31.85	20.35	2.32	0.010	0.008
2	28.68	17.57	2.57	0.020	0.018
3	27.79	18.12	2.84	0.030	0.032
4	23.59	18.46	2.80	0.040	0.036
5	19.50	17.67	2.80	0.050	0.054
6	19.60	17.72	2.90	0.060	0.062
7	19.66	17.51	2.88	0.070	0.068
8	19.07	17.55	2.97	0.080	0.083
9	19.34	19.25	3.18	0.090	0.089
10	19.68	19.83	3.29	0.10	0.098

Table 2. The five data parameters width (a), height (b), strut radii (r_1, r_2, r_3) and E_z calculated from the cubic point cloud data

Progression	Width (a)	Height (b)	r_1	r_2	r_3	E_z (Regressor)	E_z (Homogenization)
1	32.11	40.40	4.14	2.33	4.28	0.0999	0.1023
2	19.21	38.18	2.90	3.15	4.19	0.2002	0.1931
3	16.77	39.96	4.12	2.92	4.72	0.2993	0.2942
4	17.26	43.69	5.24	3.16	5.29	0.4016	0.3619
5	18.13	39.02	5.45	3.78	5.24	0.5004	0.4557
6	18.78	35.91	5.38	4.48	5.28	0.5995	0.6435
7	17.99	34.26	5.30	5.83	5.20	0.6997	0.6830
8	17.89	32.87	5.60	5.65	5.25	0.8002	0.8158
9	16.34	31.61	5.76	5.99	5.30	0.9009	0.9172

Table 3. The five data parameters width (a), height (b), strut radii (r_1, r_2, r_3) and E_z calculated from the octahedron point cloud data

Progression	Width (a)	Height (b)	r_1	r_2	r_3	E_z (Regressor)	E_z (Homogenization)
1	23.85	40.33	2.36	1.64	1.52	0.0500	0.0777
2	24.60	44.68	2.51	1.74	1.88	0.1003	0.1035
3	24.45	46.05	2.67	2.00	2.15	0.1502	0.1429
4	17.65	47.70	2.52	1.88	2.11	0.1999	0.1927
5	19.75	52.10	2.96	2.19	2.57	0.2498	0.2651
6	20.43	54.19	3.18	2.47	3.09	0.2999	0.3292